



Universiteit  
Leiden  
The Netherlands

## Fuel cell electrocatalysis : oxygen reduction on Pt-based nanoparticle catalysts

Vliet, D.F. van der

### Citation

Vliet, D. F. van der. (2010, September 21). *Fuel cell electrocatalysis : oxygen reduction on Pt-based nanoparticle catalysts*. Faculty of Science, Leiden University. Retrieved from <https://hdl.handle.net/1887/15968>

Version: Corrected Publisher's Version

License: [Licence agreement concerning inclusion of doctoral thesis in the Institutional Repository of the University of Leiden](#)

Downloaded from: <https://hdl.handle.net/1887/15968>

**Note:** To cite this publication please use the final published version (if applicable).

# Chapter 5

## Multimetallic Au/FePt<sub>3</sub> Nanoparticles as Highly Durable Electrocatalyst

We report the design and synthesis of multimetallic Au/Pt-bimetallic nanoparticles as a highly durable electrocatalyst for the oxygen reduction reaction (ORR) in proton exchange membrane fuel cells (PEMFCs). This system was first of all studied on well-defined Pt and FePt thin films deposited on a Au(111) surface, which has guided the development of novel synthetic routes toward shape-controlled Au nanoparticles, coated with a Pt-bimetallic alloy. It has been demonstrated that these multimetallic Au/FePt<sub>3</sub> nanoparticles possess both the high catalytic activity of Pt-bimetallic alloys and the superior durability of the tailored morphology and composition profile, with mass-activity enhancement of more than one order of magnitude over Pt catalysts. The reported synergy between well-defined surfaces and nanoparticle synthesis offers a persuasive approach toward nanomaterials with advanced functionality.

The contents of this chapter have been submitted: C. Wang, D. van der Vliet, K.L. More, N.J. Zaluzec, S. Peng, S. Sun, H. Daimon, G. Wang, J. Greeley, J. Pearson, A.P. Paulikas, G. Karapetrov, D. Strmcnik, N.M. Markovic and V. R. Stamenkovic, *Nano Lett.*, (2010)

## 5.1 Introduction

Fuel cell technology is believed to be the next generation of energy solutions for powering stationary systems, portable electronic devices and vehicles. [1] With hydrogen as a fuel, this technology is environmentally friendly, as it generates electricity from the hydrogen oxidation reaction at the anode and oxygen reduction reaction (ORR) at the cathode, producing water as the only by-product. Platinum in the form of nanoparticles dispersed on a high surface area carbon matrix is considered to be the catalyst of choice for these two reactions. [2] However, Pt that is in general chemically inert becomes unstable when exposed to the hostile electrochemical environments where Pt surface atoms dissolve and migrate, resulting in aggregation of nanoparticles and loss of surface area, activity and power density. [3] Specifically, the instability of Pt at the cathode side represents one of the major limitations for commercialization of this technology.

Numerous research efforts have indicated that the activity of Pt catalysts can be improved by alloying Pt with transition metals such as Fe, Co or Ni. [4-13] In recent studies we examined the extended surfaces of these alloys, and reported that the high activity originated from the modified electronic structures of Pt, which altered the adsorption of spectator species from the electrolyte and the binding energies of key reaction intermediates, and thus improved the reaction kinetics. [12-15] Despite the quest for more active systems, the stability of catalysts is less well investigated, with the exception of a few studies that have offered some promising directions. [3, 16, 17] It has also been reported that Pt surface sites with low coordination numbers, such as step edges, corners, kinks, and adatoms, are more vulnerable to dissolution than the atoms arranged in the long-range ordered (111) or (100) facets [18], as confirmed by scanning tunnelling microscopy (STM) studies combined with electrochemical and infrared characterizations of Pt single crystal surfaces covered with adsorbed CO. [19] In all cases it has been found that the adsorption of surface oxides takes place first on the low-coordinated Pt sites. Once formed, the rather strong Pt-oxide interaction induces substantial morphological changes of the topmost Pt layer, triggering the decay in fuel cell performance. Therefore, it becomes necessary to study the catalytically active materials on a more fundamental level in order to develop advanced catalysts with not only high activity, but also superior durability.

Considering that Pt-bimetallic materials have been extensively investigated it is plausible to propose that multimetallic systems could offer unprecedented benefits in catalysis by bringing together, in a controlled manner, highly diverse constituents that might be utilized to alter and tune not only catalytic properties, but the durability of the catalyst as well. Here we present an advanced catalyst based on multimetallic Au/FePt nanoparticles (NPs), which is catalytically active and highly durable for the ORR. The choice of elements was partially based on the recent reports of composite nanostructures for catalytic applications [20, 21], but more on our earlier studies of monodisperse Au NPs [22], Au single crystals modified with Pd thin films [23], and Pt-bimetallic alloys. [12, 13] The initial experiments were carried out on well-defined surfaces of binary Au(111)-Pt and ternary Au(111)-FePt systems. The obtained fundamental insight into the synergy between these materials has enabled us to resolve, define and utilize the exact role of each constituent in a ternary system. This has guided the synthesis of tailored NPs possessing favorable coordination of surface active sites, distribution of elements and amount of Pt in the system.

## 5.2 Results

Thin films of bimetallic FePt<sub>3</sub> (and/or Pt) were deposited in vacuum over a Au(111) substrate. The film thickness was chosen to be approximately five atomic layers in order to mimic the advanced catalytic properties of the nanosegregated concentration profile previously established for bulk Pt-bimetallic alloys. [12]

Figure 5.1 summarizes the results from the rotating disk electrode (RDE) measurements obtained for these thin films and demonstrates that, in accordance with the electrochemical properties of individual elements, addition of each of these metals induces extra functionality in the catalyst: *i*) Au is chemically stable in acidic electrolyte and electrochemically inactive for the ORR ( $E > 0.6$  V). Au is also inert towards the adsorption/desorption processes of underpotentially deposited hydrogen  $H_{\text{upd}}$  (region I) and surface oxides  $OH_{\text{ad}}$  (region III, the potential range of interest for the ORR), although the latter is evident in region IV between  $1.2 < E < 1.6$  V; *ii*) Pt is the only metal in this system that adsorbs underpotentially deposited hydrogen ( $H_{\text{upd}}$ ) (region I) and is active for the ORR with respectable, but not satisfactory stability; *iii*) addition of Fe atoms in an alloy with Pt is known to induce catalytic enhancements for the ORR. [13]

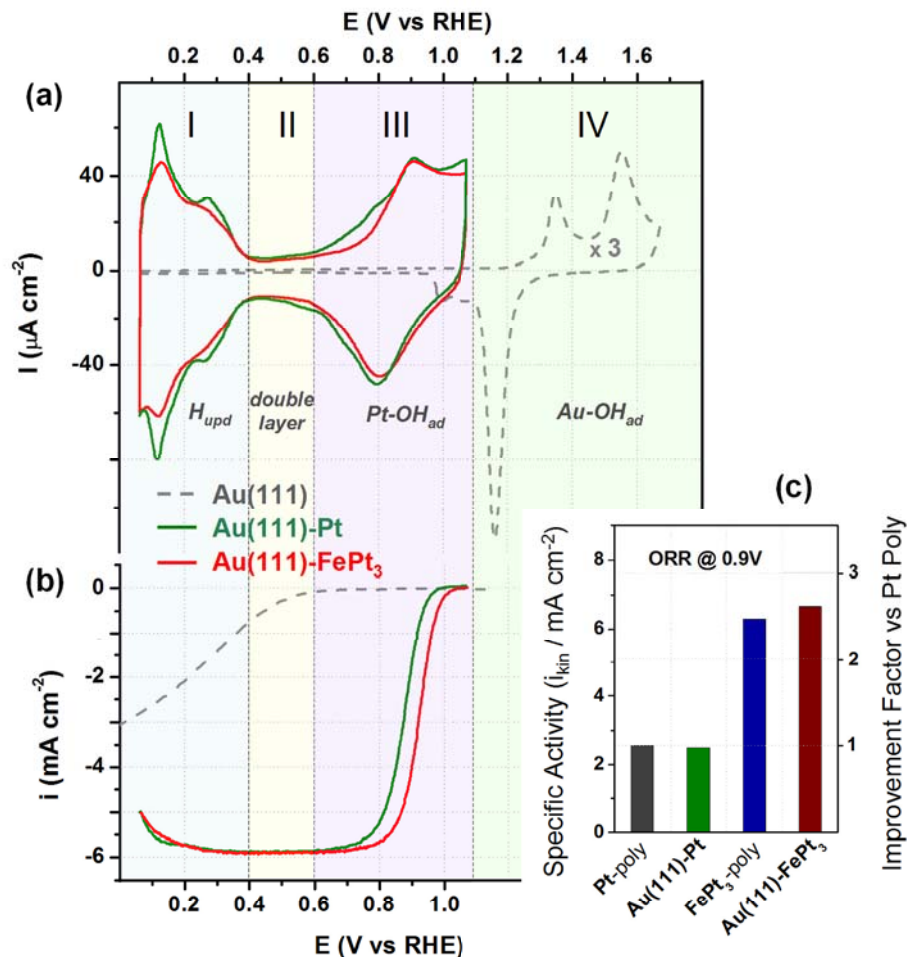


Figure 5.1. Electrochemical RDE characterization of Au(111) surface (gray) and Pt (green), FePt<sub>3</sub> (red) thin film surfaces supported on Au(111) substrate in 0.1M HClO<sub>4</sub>: (a) cyclic voltammograms show that the onset of oxide adsorption on Au is positively shifted by more than 600 mV vs. Pt, indicating that Pt is much more oxophilic than Au; (b) polarization curves for the ORR at 1600 rpm and (c) summary of specific activities for the ORR@0.9 V vs. RHE, at 60°C with 1600 rpm with a sweep rate of 50 mV/s.

The voltammograms depicted in Figure 5.1a reveal that Pt is much more oxophilic than Au, which is clearly visible from the difference in the onset potential of oxide adsorption (a positive shift by 600 mV on Au vs. Pt demonstrates that Au is more difficult to be oxidized than Pt). The same figure also shows Pt-like behavior of the Au(111)-Pt and Au(111)-FePt<sub>3</sub> thin film surfaces with pronounced  $H_{upd}$

peaks (region I) as well as Pt-oxide adsorption/desorption peaks in the potential region III  $0.6 < E < 1.1$  V. Moreover, the differences in voltammetry between Pt and FePt<sub>3</sub> thin film surfaces are clearly visible, *i.e.*, suppressed H<sub>upd</sub> region and positive potential shift of the onset of surface oxide formation for Au(111)-FePt<sub>3</sub>. [12, 13] Consequently, this is reflected by a considerably improved (~2.5 fold) specific catalytic activity for the ORR measured on the Au(111)-FePt<sub>3</sub> surface. There was no change in activity between Pt-poly and Au(111)-Pt electrodes, implying that the Au substrate does not alter the adsorption/electronic/catalytic properties of the outermost Pt atoms (figure 5.1b and 5.1c).

In addition to the improvement in activity, it was also found that the ternary system exhibited high stability during the electrochemical experiments (see section 5.7, figures 5.14-5.17). Prolonged electrochemical characterizations and measurements at extremely high overpotentials relevant for the oxygen evolution reaction have indicated the absence of Au atoms on the surface (Figure 5.18 and 5.19). Regardless of the temperature range (20 to 60°C) or potential limit (which was as high as ~1.7 V versus the reversible hydrogen electrode, RHE), the surface did not suffer any change in composition. Based on the fundamental properties of Au and Pt, it is always expected to have diffusion of Au bulk atoms toward and over Pt surface atoms due to the difference in surface segregation energies. [24] However, this was not the case for Pt or Pt-bimetallic thin films on the Au substrate. These results provide important insights and show that the multimetallic system, comprised of a Pt/Pt-bimetallic surface layer over a Au substrate, is highly stable, despite the standard thermodynamic arguments mentioned above.

Several essential findings were obtained from the well-defined extended ternary systems such as: *i*) the multilayered Pt-bimetallic thin film could govern the catalytic properties to the same extent as in the case of bulk Pt-bimetallic systems; *ii*) the Au substrate could replace buried non-functional Pt atoms; *iii*) an electrochemically more inert Au substrate could facilitate the stabilization of the topmost Pt atoms. These findings were used as a guide in designing and synthesizing an advanced nanoscale electrocatalyst. In order to synthesize multimetallic NPs with the preferred surface coordination and concentration profile, we aimed toward shape-controlled Au NPs coated with a Pt-bimetallic alloy. [25-27]

### 5.3 Core shell particle synthesis and analysis

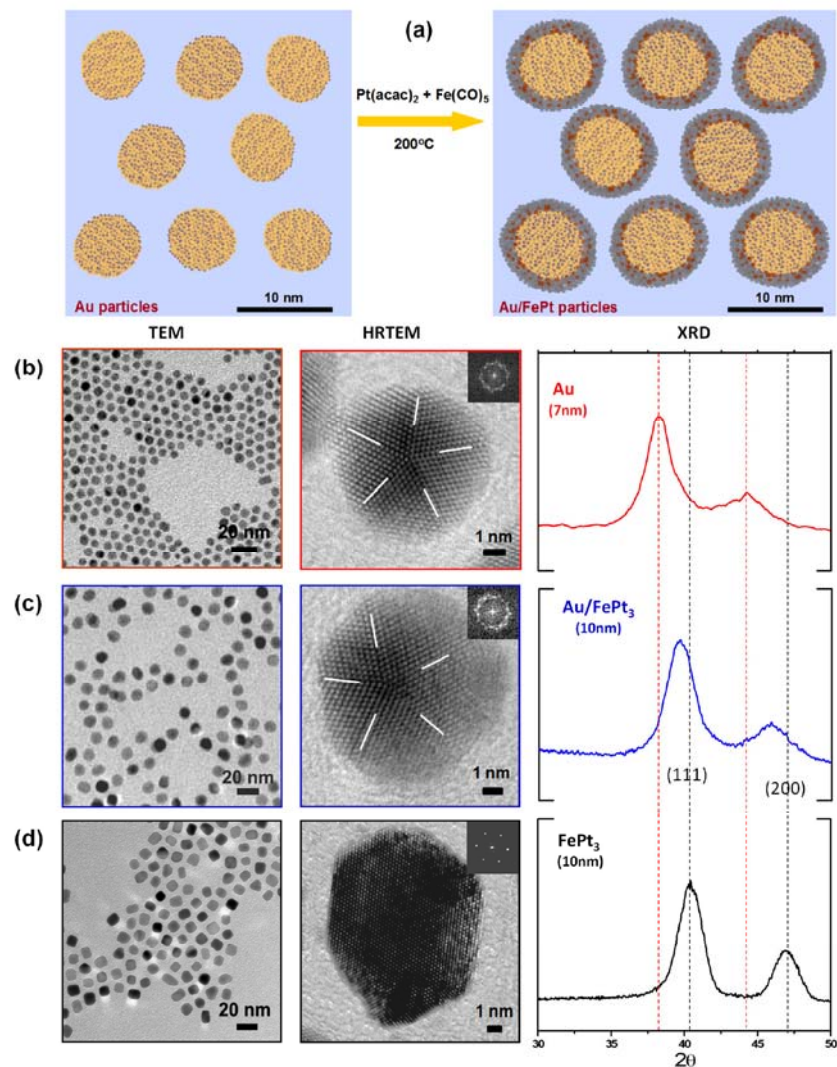


Figure 5.2. Synthesis and characterization of core/shell Au/FePt<sub>3</sub> NPs. (a) Schematic illustration of core/shell Au/FePt<sub>3</sub> NPs synthesis. TEM, HRTEM and XRD characterization of: (b) 7 nm Au, (c) 7/1.5 nm core/shell Au/FePt<sub>3</sub> NPs and (d) 10 nm FePt<sub>3</sub>. The twinning boundaries for five-fold symmetry axes were marked by dash lines in the HRTEM images of Au and Au/FePt<sub>3</sub> NPs, where the insets show their respective fast Fourier transform (FFT) patterns with multi-fold symmetry clearly identified. The positions of (111) and (200) peaks for Au (red) and FePt<sub>3</sub> (black) are marked with dotted lines respectively in the XRD patterns.

Au NPs were prepared via the reduction of chloroauric acid (HAuCl<sub>4</sub>) by *Tert*-butylamine-borane at room temperature [22], while epitaxial coating by FePt<sub>3</sub> was done by mixing Au NPs with platinum acetylacetonate, Pt(acac)<sub>2</sub>, at 120°C in the presence of oleic acid and oleylamine, followed by adding Fe(CO)<sub>5</sub> and further growth at 200°C (Figure 5.2a). The molar ratio of Fe(CO)<sub>5</sub> to Pt(acac)<sub>2</sub> was adjusted to control the composition of the coating,[28] with a ratio of 0.8 : 1 giving Fe : Pt = 1 : 3 (Figure 5.12 and 5.20). Similar synthetic conditions without Au seeds were used to obtain Pt and FePt<sub>3</sub> NPs of the same size in order to eliminate particle size effect [29-32] in the following study. As-synthesized NPs were incorporated into carbon black (900 m<sup>2</sup>/g), and the organic surfactants were removed by heating the NPs/carbon mixture in oxygen rich atmosphere.

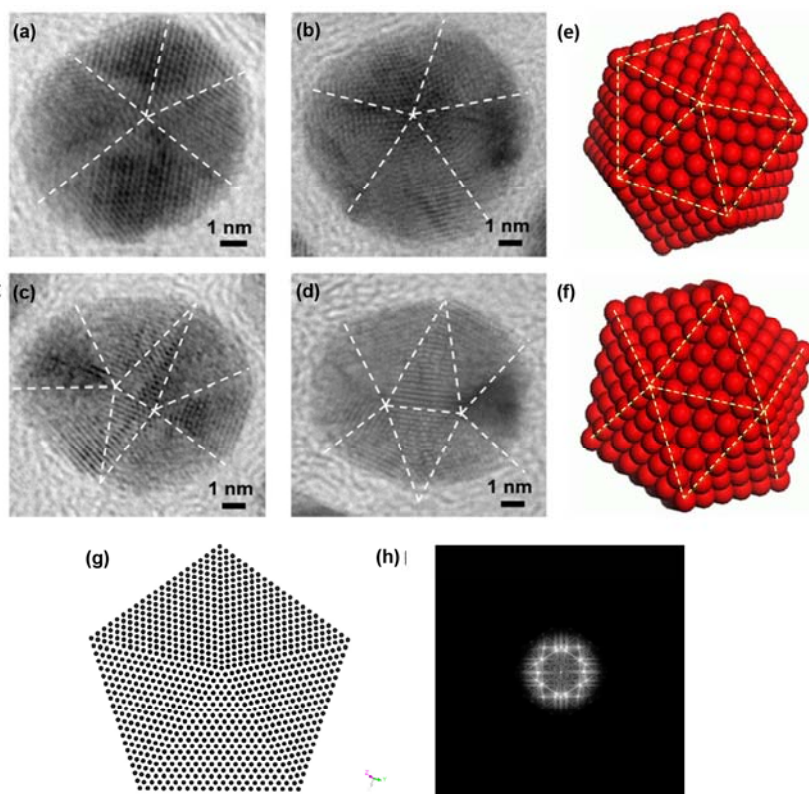
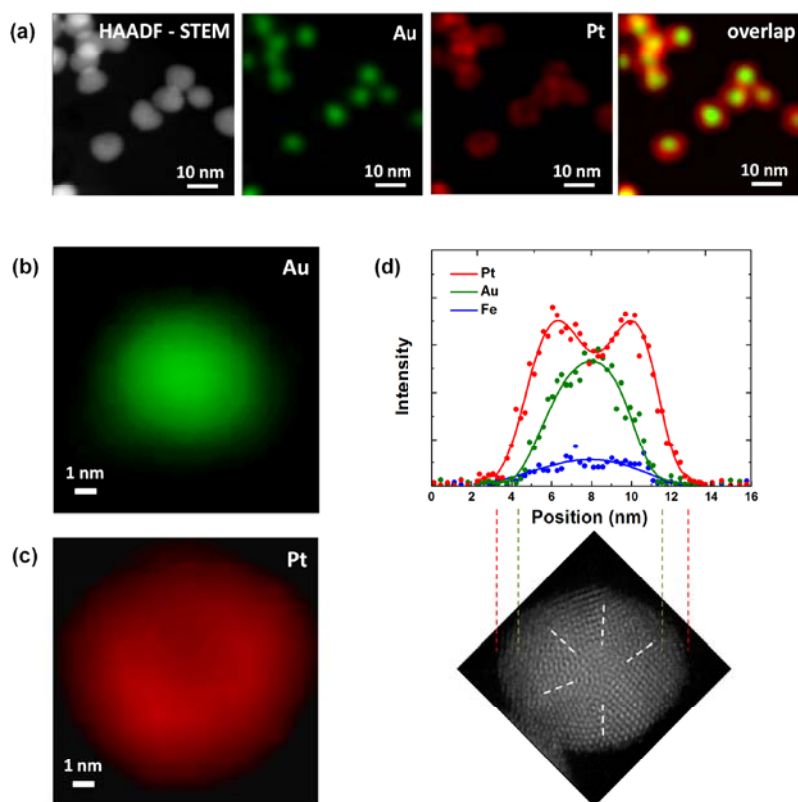


Figure 5.3. (a – d) Representative HRTEM images of icosahedral Au/FePt<sub>3</sub> NP viewed along different directions with (e, f) the corresponding orientation of model particles. (g) The arrangement of atoms extracted from the facets around a five-fold symmetry axis of an icosahedron and (h) its FFT pattern. The multi-fold symmetry in the FFT pattern can be comparable with those shown in Figure 5.2.

Figure 5.2 depicts the morphology, structure and size of the Au/FePt<sub>3</sub> NPs with the standard deviation in size distribution less than 5%. The average diameter of the monodisperse Au NPs increased from 7 to 10 nm after the FePt<sub>3</sub> coating (figure 5.2b), indicating that a 1.5 nm thick layer has been deposited over the Au seeding NPs (Figure 5.2c). High resolution TEM (HRTEM) images in figure 5.2 reveal substantial differences in morphology among the particles. The Au NPs possess an icosahedral shape [22] while the FePt<sub>3</sub> NPs have a cubo-octahedral shape that is typical for Pt and Pt-bimetallic NPs. From figure 5.2 it is also obvious that the icosahedron-like morphology of the Au seeds is retained after coating with the FePt<sub>3</sub>, as evidenced by the presence of fivefold symmetry axis, which is considered to be the characteristic feature of this type of morphology (figure 5.2c and 5.3).[33-35]



**Figure 5.4.** Elemental distribution analysis of core/shell Au/FePt<sub>3</sub> NPs: (a) HAADF-STEM characterization and elemental mapping of Au (green), Pt (red) and their overlap; (b), (c) the elemental maps of Au and Pt for a single core/shell particle and (d) line profile - elemental distribution along a single particle.

Although it is difficult to distinguish Au from Pt in HRTEM images (figure 5.2c) due to the negligible contrast between these two elements, the concentration profile of multimetallic particles was established by elemental analysis carried out by scanning transmission electron microscopy (STEM). Figure 5.4a shows the high angle annular dark field (HAADF) STEM image and elemental mapping of Au and Pt in the NPs, indicating that Au (green) is surrounded by Pt (red) (additional images are given in figure 5.5; however, the signal for Fe is rather weak and mapping of Fe is statistically challenged). Figure 5.4b and 5.4c present elemental mapping of Pt and Au in a single ~10 nm NP, while figure 5.4d shows the line profiles for all three elements obtained by scanning e-beam across the NP. It can be seen that the Au peak (green line) is about 3 nm narrower than the Pt peak (red line), confirming the coating thickness of about 1.5 nm.

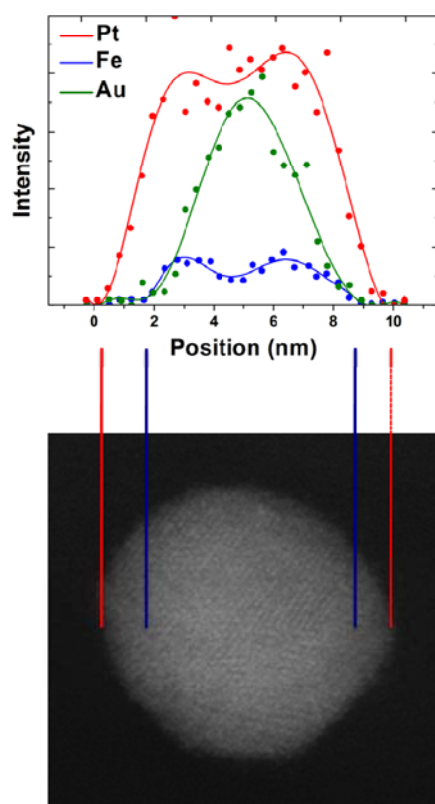
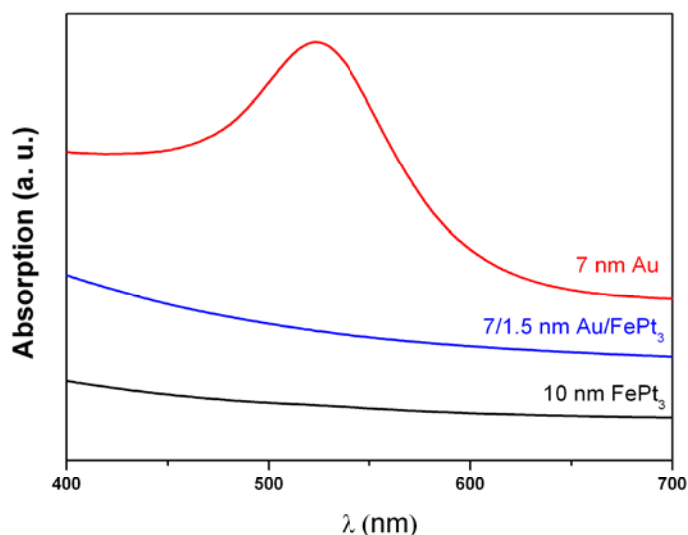


Figure 5.5. More images for element mapping of Au/FePt<sub>3</sub> NP by HAADF-STEM. The concentration profile is clearly seen by the overlapping image (left) of Pt and Au. Below, additional line profile is given for a single Au/FePt<sub>3</sub> particle that reveals the coating thickness and its concentration profile.

The concentration profile was also verified by the structural and optical characterizations of the Au/FePt<sub>3</sub> NPs. The X-ray diffraction (XRD) patterns of the Au seeds, Au/FePt<sub>3</sub> and FePt<sub>3</sub> NPs have typical peaks of fcc crystals (Figure 5.2 and S11). By taking a close view of the XRD patterns, we find that the (111) peak of Au/FePt<sub>3</sub> NPs is downshifted compared to that of FePt<sub>3</sub> NPs, and the spacing between the adjacent (111) planes are calculated to be 0.235 nm, 0.227 nm and 0.223 nm for Au, Au/FePt<sub>3</sub> and FePt<sub>3</sub> NPs respectively according to Bragg's law. A similar trend can also be established for (200) and other peaks. This observation implies that the average Pt-Pt bonding length in the Au/FePt<sub>3</sub> NPs is slightly larger than that in FePt<sub>3</sub> NPs. Such an increase of metallic bonding radius in the coated FePt<sub>3</sub> could originate from alloying at the Au/FePt<sub>3</sub> interface where no clear boundary exists and an intermixed phase is formed between Au and FePt<sub>3</sub> (which has also been confirmed by HAADF STEM analyses, figure 5.8). Additionally, optical properties of Au/FePt<sub>3</sub> NPs were investigated by UV-Vis spectroscopy (figure 5.6). The 7 nm Au NPs have a strong surface plasmonic absorption peak at 520 nm. [36] In contrast, the Au/FePt<sub>3</sub> NPs show a featureless spectrum similar to the FePt<sub>3</sub> NPs. This, plus the elemental analysis, proves that the Au seeds are entirely coated by FePt<sub>3</sub> in the multimetallic NPs.



**Figure 5.6.** UV-vis spectra of Au/FePt<sub>3</sub> and Au NPs dispersed in hexane. 7 nm Au NPs show a surface plasmon resonance peak around 520 nm, but Au/FePt<sub>3</sub> NPs have no visible feature in the UV-vis spectrum (just like FePt<sub>3</sub> NPs). This confirms that the Au seeds were entirely coated by FePt<sub>3</sub>, and no Au atoms are present on the surface of multimetallic particles.

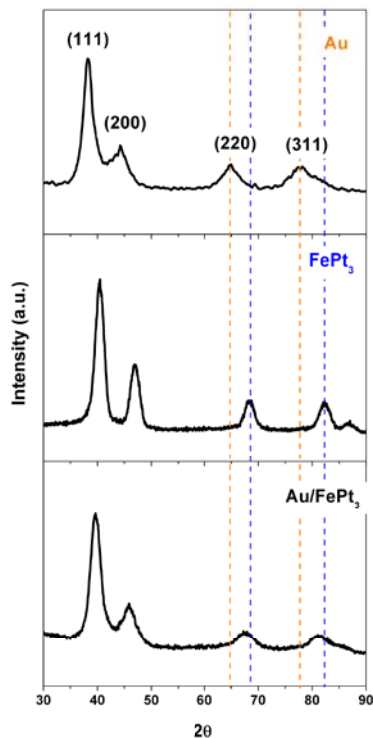


Figure 5.7. Whole range of XRD patterns for Au, FePt<sub>3</sub>, and Au/FePt<sub>3</sub> NPs. In addition to (111) and (200) peaks shown in Figure 5.2, shift for high-angle peaks (220) and (311) are marked here (dashed lines: orange for Au, and blue for FePt<sub>3</sub>). Particularly, the pattern for Au/FePt<sub>3</sub> NPs shows no extra peak at the positions of Au (220) and Au (311) peaks, indicating neither free Au nor dimmer-like Au-FePt<sub>3</sub> NPs exist after coating.

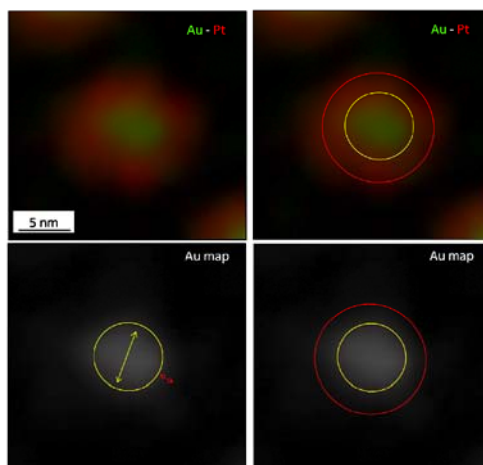


Figure 5.8. HAADF-STEM analysis of the interfacial alloying in the Au/FePt<sub>3</sub> NPs. The Au map shows ~5nm core of pure Au (yellow) and ~1 nm thick layer of mixed Au-Pt-Fe (red).

## 5.4 Electrochemical characterization

Electrochemical characterization of the NPs was done by RDE with a glassy carbon disk (figure 5.9). Based on the cyclic voltammograms obtained for different catalysts the Au/FePt<sub>3</sub> behaves just like Pt and FePt<sub>3</sub> NPs, indicating that the multimetallic particles have a Pt-rich surface. The catalytic performance of Au/FePt<sub>3</sub>/C for the ORR is similar to its bimetallic counterpart FePt<sub>3</sub>/C, with an improvement factor of > 3 versus Pt/C catalyst, which is consistent with the results measured on well-defined extended surfaces. Additional insights for the Au/FePt<sub>3</sub>/C NPs were obtained from the electrochemical CO oxidation and cyclic voltammetry by opening potential up to 1.7 V (figure 5.21). A perfect match between H<sub>upd</sub> and CO stripping charge combined with the absence of Au redox peaks at 1.35 and 1.15 V prove that there is no presence of Au atoms on the surface of the multimetallic particles. The electrochemical results indicate that a highly efficient chemical coating of the Au substrate has produced a homogeneous layer of the Pt-bimetallic alloy without Au atoms in the topmost surface layer.

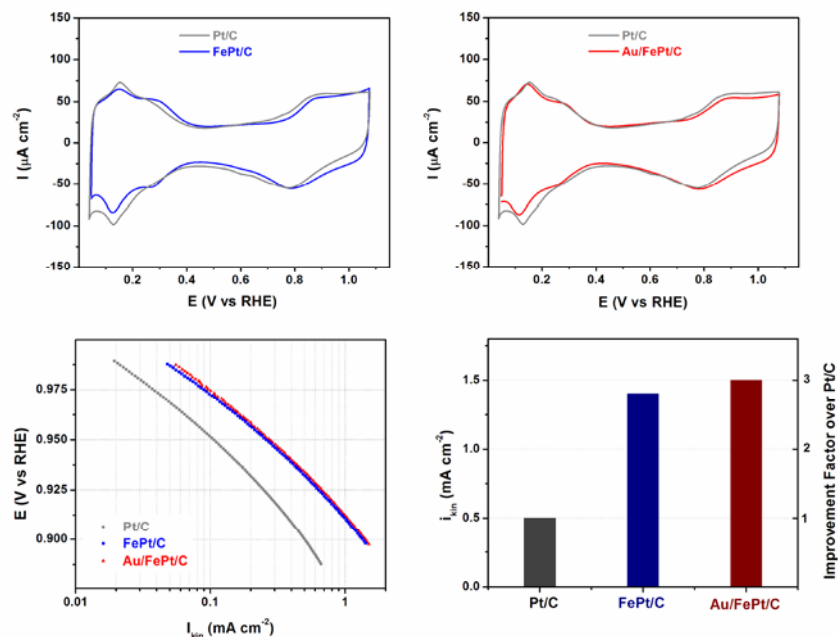


Figure 5.9. Electrochemical RDE characterization of Pt/C (grey), FePt<sub>3</sub>/C (blue) and Au/FePt<sub>3</sub>/C (red) catalysts in 0.1M HClO<sub>4</sub>: (a), (b) cyclic voltammograms, (c) specific activities at 1600 rpm for the ORR at different electrode potentials (Tafel plot) and (d) summary of specific activities for the ORR@0.9 V vs. RHE, at 60°C with 1600 rpm with a sweep rate of 20 mV/s.

The most vital feedback from the electrochemical characterization has been obtained from the durability measurements. These experiments were designed to imitate the operating conditions of fuel cells and were carried out by cycling the potential between 0.6 V and 1.1 V (versus RHE) in an oxygen saturated electrolyte. Figure 5.10a-c shows the summary of the electrochemical properties of Au/FePt<sub>3</sub>/C compared with Pt/C and FePt<sub>3</sub>/C before and after 60,000 potential cycles. No significant loss in surface area or specific activity was observed for Au/FePt<sub>3</sub>/C, in contrast to FePt<sub>3</sub>/C and Pt/C. Of particular note is that the initial specific activity of the Au/FePt<sub>3</sub>/C catalyst was as high as that of FePt<sub>3</sub>/C, but after the potential cycling the activity of FePt<sub>3</sub>/C dropped much more than the activity of Au/FePt<sub>3</sub>/C did. After the potential cycling the multimetallic catalyst has 7 times higher specific activity, and more than one order of magnitude higher mass activity than Pt/C.

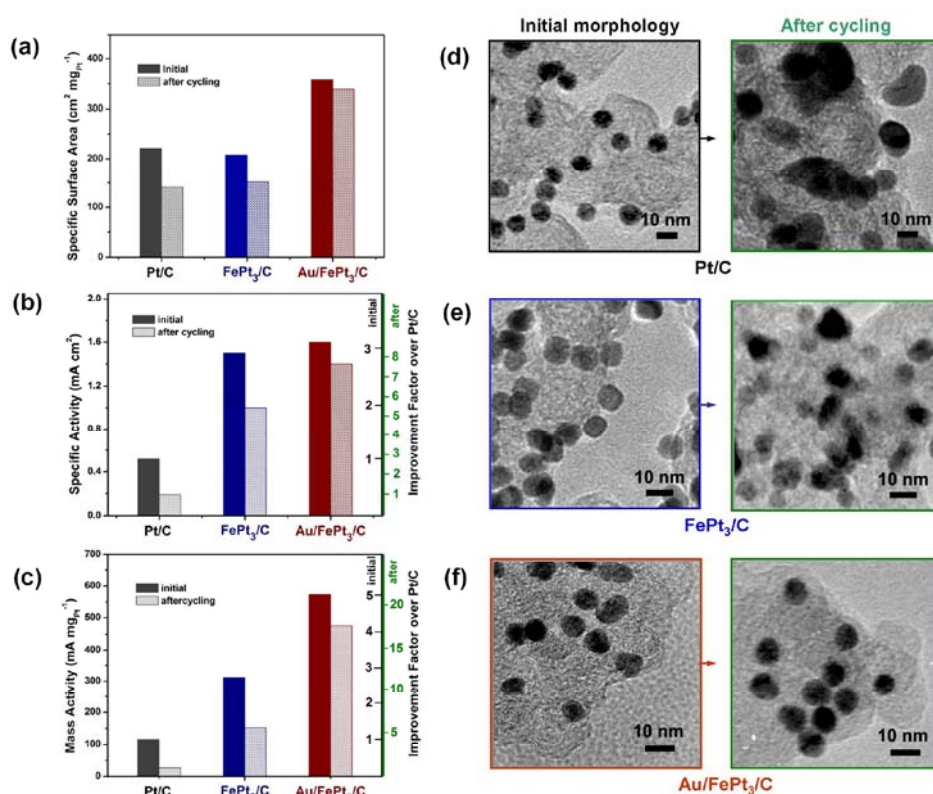
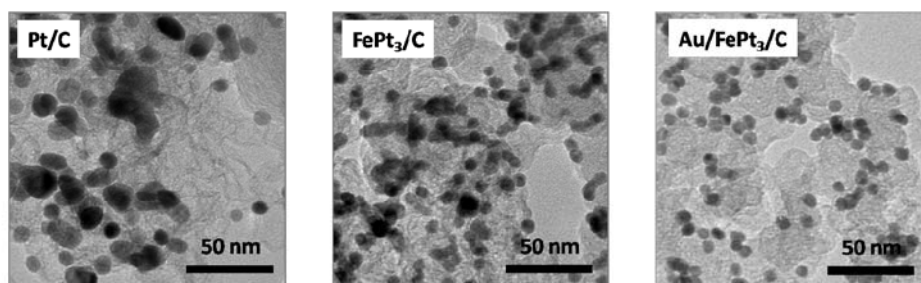


Figure 5.10. Stability characterization of the Pt/C, FePt<sub>3</sub>/C and Au/FePt<sub>3</sub>/C catalysts by 60,000 potential cycles between 0.6 V and 1.1 V vs. RHE in oxygen saturated 0.1 M HClO<sub>4</sub> electrolyte at 20°C with a sweep rate of 50 mV/s: (a-c) Summary of the specific surface area, specific and mass activities and (d-f) TEM characterization of the catalysts before and after the potential cycling.

In order to understand the enhanced stability of Au/FePt<sub>3</sub>/C catalyst and get detailed insight into the degradation mechanism, TEM characterization was performed before and after the stability studies (figure 5.10d-f). No observable change can be seen for Au/FePt<sub>3</sub> NPs before and after the 60,000 potential cycles, neither in size nor shape (figure 5.10f and TEM images in figure 5.11). However, after the potential cycles, the size of Pt and FePt<sub>3</sub> NPs has been substantially changed (Figure 5.10d and 5.10e). Big particles of over 20 nm in diameter are formed, due to the Pt instability and well-known phenomena of Ostwald ripening during electrochemical cycling. [3] These results provide remarkable evidence for the devastating morphology changes suffered by FePt<sub>3</sub>/C and Pt/C catalysts, which have had a direct influence on the decay in catalyst performance. On the contrary, the multimetallic Au/FePt<sub>3</sub> NPs do not suffer from any obvious change in morphology or performance, and represent a highly durable electrocatalyst for the ORR.



**Figure 5.11.** TEM images of the three catalysts after the stability test of 60,000 cycles from 0.6V to 1.1V vs. RHE. In the case of Au/FePt<sub>3</sub>/C, though some NPs stack together, they can still be individually distinguished from each other.

## 5.5 Discussion

Since the catalytic activity of Au/FePt<sub>3</sub>/C is at the same level as that for FePt<sub>3</sub>/C, it is not likely that the Au core directly affects the electronic/adsorption/catalytic properties of the surface Pt atoms. This is consistent with what we observed in thin films, *i.e.*, the activity of a Au(111)-Pt surface did not differ from that of a Pt-poly surface, suggesting unchanged electronic properties of the topmost Pt atoms. For that reason, the mechanism of stability improvement observed in the Au/FePt<sub>3</sub> system should be considered as being due to the synergy between the particle morphology and its unique concentration profile. Thus it is plausible to propose that

the Au core plays a key role in the durability enhancement while the topmost Pt atoms, electronically altered by the subsurface Fe, provide the high catalytic activity.

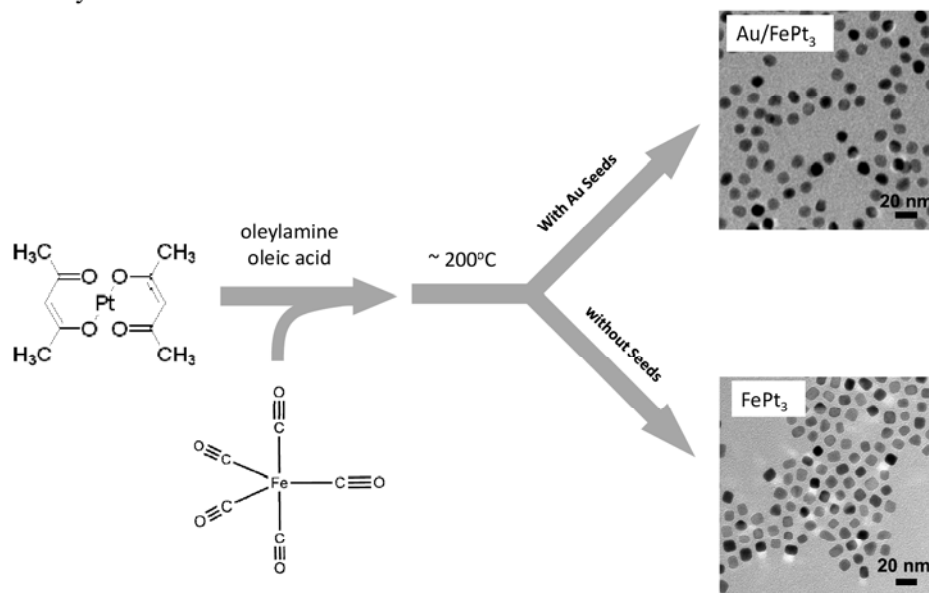


**Figure 5.12.** Scheme of Au/FePt<sub>3</sub> NP synthesis. Pt(acac)<sub>2</sub> was thermally reduced by oleylamine to Pt, and simultaneously Fe(CO)<sub>5</sub> decomposed to Fe. Pt and Fe nucleated (coated) over Au seeds into Au/FePt<sub>3</sub> NPs. In the absence of Au seeds, FePt<sub>3</sub> NPs can grow under the same synthetic conditions and size can be controlled.

As discussed above, we have demonstrated the control of morphology through seed-mediated growth using the distinctive icosahedral Au seeds; direct synthesis without Au seeds produced FePt<sub>3</sub> NPs of cubo-octahedral shape (figure 5.12), the most common morphology for Pt and Pt-bimetallic catalysts reported in the literature.

Considering that surface atom solubility is highly dependent on its coordination number (the number of nearest neighbors) [18, 29, 37], the low-coordinated atoms are more sensitive to oxidation and dissolution in electrochemical environments. [18, 19] In particular, an atom on a (111) facet has a coordination number of 9, versus 8 for (100) facets, 7 for edge sites and 6 for corner sites on a cubo-octahedral particle (figure 5.13). Correspondingly, the spatial arrangement of the topmost atoms in an icosahedron-like particle would diminish the number of low-coordinated surface sites and increase surface average coordination number compared to cubo-octahedral particles (figure 5.13 and 5.22), *e.g.*, 12 atoms with

the coordination number of 6 on an icosahedron vs. 24 on a cubo-octahedron. Therefore, it is reasonable to expect that the surface atoms of an icosahedron-like Au/FePt<sub>3</sub> NPs are less vulnerable to dissolution than those of cubo-octahedral FePt<sub>3</sub> NPs, thus enhancing the durability of the multimetallic catalyst.

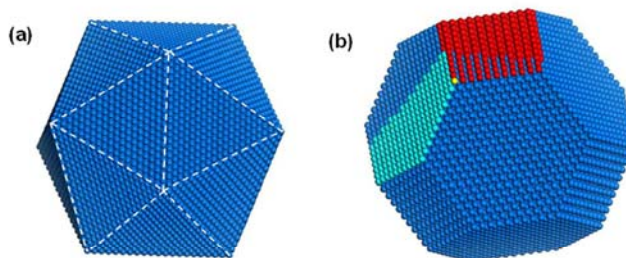


**Figure 5.13.** The detailed analysis of the coordination number distribution of Pt surface atoms of a 10 nm NP in (a) icosahedral or (b) cubo-octahedral shape. There are 29881 atoms in the cubo-octahedral NP, and 28741 atoms in the icosahedral NP. Stastical results (listed in section 5.7) show that the surface of icosahedron has higher average coordination number than that of cubo-octahedron.

In accordance with surface segregation energies in transition metals [38], a gold enriched surface would be expected in this system. However, no trace of surface Au was found from elemental mapping and electrochemical measurements, signifying that the stable topmost layer consists of Pt atoms only, while interfacial alloying between the Au core and the Pt-bimetallic shell might occur in the subsurface layers. A similar divergence in surface composition from the thermodynamically favorable state was also reported for Rh/Pd core/shell NPs, and it was found to be strongly dependent on the nature of the reactive environment. [24] For the given electrochemical conditions, apparently Pt is easier to be oxidized than Au (figure 5.1), which provides the driving force for Pt atoms to stay on the surface in a highly oxophilic environment. Therefore, we propose here that the counterbalance between the two opposing forces; the rather strong interaction between Pt and surface oxides on one side, and the tendency of Au to segregate over Pt on the other side, have induced another beneficial stabilization mechanism of the topmost Pt layer (figure 5.23 and 5.24). It turns out that these two opposing energetic driving forces are of comparable magnitude, according to first-principles calculations. In particular, the surface-adsorbed O or OH groups, in proximity to Au atoms (for example, at sufficiently high O coverages), can reverse the thermodynamic driving force for Au to segregate to the surface of a Pt lattice. In effect, as discussed above,

the energetic preference for Au to be on the surface of Pt in vacuum is cancelled out by the reduced affinity of Au for adsorbed oxygen containing species. These results, in turn, imply that Au will remain below the Pt surface during electrochemical operation at potentials sufficiently high to cause adsorption of oxygen containing species. Thus, the adsorbate-induced segregation has led to the formation of a Pt-skin layer, which is electronically/catalytically altered by subsurface Fe while stabilized by subsurface Au.

The existence of subsurface Au atoms makes an additional contribution to the durability enhancement of the Pt skin layer by modifying the well-known place-exchange mechanism.[18, 39] This mechanism operates for Pt at electrode potentials relevant to the ORR and involves migration of atomic oxygen from surface to subsurface positions. Place-exchange is considered to be one of the precursors for Pt dissolution, yet in the case of Au/FePt<sub>3</sub> particles it is effectively hindered due to the presence of Au atoms in subsurface layers, i.e., Au cannot be oxidized in the given potential range that is relevant for the ORR (see figure 5.1a, potential regions III and IV), and therefore, occurrence of Au in the subsurface layers would make the formation of subsurface oxides less energetically favorable and hence suppress the dissolution of Pt (Figure 5.25). Supplementary evidence in support of this mechanism has been obtained through a Density Functional Theory (DFT) model of subsurface atomic oxygen adsorption in FePt<sub>3</sub>(111) alloys (figure 5.26). When a Au atom is substituted for Pt in the subsurface layer, the strength of subsurface oxygen binding decreases in magnitude by about 0.15 eV. This decrease is expected to make oxygen place exchange thermodynamically less feasible, thereby reducing Pt loss in the ternary system under this well-known Pt-dissolution mechanism.

Although there is the effect of particle morphology and surface coordination, we believe that the unique compositional profile of Au/FePt<sub>3</sub> NPs should be the dominant factor contributing to the observed durability enhancement, as it alternates the energetics and kinetics related to the dissolution processes of Pt in the electrochemical environments, which is revealed by our first-principle theoretical studies. The proposed durability enhancement in this study is quite unique, and differs from the recent report in which Au nanoclusters were deposited on Pt particle surface. [16] In that case the stability enhancement was assigned to the raised oxidation potential of Pt by Au. In contrast, the ternary catalyst described here does not suffer any loss of Pt active sites due to the presence of surface Au clusters and thus provides highly efficient utilization of Pt. The fine balance among the key factors such as the proper order of synthesis steps, stoichiometric ratio

between the elements, and the temperature for FePt overgrowth have enabled the formation of NPs with controlled shape, size, and composition profile, which do not only preserve the beneficial catalytic properties of Pt-bimetallic alloy surfaces, but also exhibit superior durability performance by using a minimal amount of Pt in the system. Most significantly, the dramatic activity enhancement is illuminated by the improvement factors of over 7 in specific activity and more than one order of magnitude in mass activity for Au/FePt<sub>3</sub>/C versus Pt/C after extensive potential cycling.

## 5.6 Summary

In summary, we have developed a synergistic approach toward advanced fuel-cell catalysts by combining the studies of well-defined surfaces and nanomaterial synthesis. Based on the knowledge gained from FePt thin films deposited on Au single-crystal substrates, tailored Au/Pt-bimetallic nanoparticles have been designed and synthesized by an organic solvothermal method. The morphology control and preferred composition profile were achieved through epitaxial growth of Pt-bimetallic alloy over Au seeds. Compared to FePt<sub>3</sub>/C and Pt/C, the multimetallic Au/FePt<sub>3</sub> catalyst showed superior durability while preserving the beneficial catalytic activity of Pt-bimetallic alloys. This work reveals the great potential of utilizing multimetallic nanostructures in tuning the catalytic and durability properties of nanocatalysts. The developed synergistic strategy reported here could also be generalized to connect fundamental studies and novel nanomaterial synthesis for advanced catalytic and other applications.

## **5.7 Appendix**

### **5.7.1 Part 1 Experimental Methods and Characterizations**

#### **5.7.1.1 Nanoparticle Synthesis**

##### **5.7.1.1.1 7 nm Au NPs**

A solution of 10 ml 1,2,3,4-Tetrahydronaphthalene (tetralin, anhydrous 99%, Sigma-Aldrich), 10 ml oleylamine (70%, Sigma-Aldrich), and 0.1 g H<sub>2</sub>AuCl<sub>4</sub>·3H<sub>2</sub>O (99.9985%-Au, Strem) was prepared in air at 15°C and magnetically stirred under N<sub>2</sub> flow. 0.5 mmol of Tert-butylamine-borane (97%, Sigma-Aldrich) complex was dissolved in tetralin (1 mL) and oleylamine (1 mL) and injected into the precursor solution. The reaction initiated instantaneously and the solution changed to a deep purple color within 5 s. The mixture was allowed to be aged at 15°C for 1 h before 60 ml acetone (ACS grade, BDH) was added to precipitate the Au NPs. The Au NPs were collected by centrifugation (8500 rpm, 8 min), washed with acetone and redispersed in hexane (ACS grade, BDH).

##### **5.7.1.1.2 7/1.5 nm Au/FePt<sub>3</sub> NPs**

30 mg of 7 nm Au NPs were mixed with 10 ml octadecene (90%, Sigma-Aldrich), 0.1 g Pt(acac)<sub>2</sub> (98%, Strem), 1 ml oleylamine and 1 ml oleic acid (90%, Sigma-Aldrich) at 120°C. 0.03 ml Fe(CO)<sub>5</sub> (99.5%, Strem) was added under N<sub>2</sub> atmosphere, then the temperature was raised to 200°C. The solution was cooled down to room temperature after 30 minutes. 50 ml iso-propanol (99.5%, Sigma-Aldrich) was added to precipitate the NPs and the product was collected by centrifuge (6000 rpm, 5 min). The obtained Au/FePt<sub>3</sub> NPs were washed with ethanol (denatured ACS grade, BDH) and redispersed in hexane. Similar recipe without adding Au seeds was used to synthesize 10 nm FePt<sub>3</sub> NPs. Synthesized NPs were incorporated into carbon black (900 m<sup>2</sup>/g), and the organic surfactants were removed by heating the NPs/carbon mixture in oxygen rich atmosphere. Total metal loading was adjusted to be 20% for all catalysts used in this work.

### 5.7.1.2 Material Characterizations

TEM images were collected on a Philips EM 420 (120 kV). HRTEM images were recorded using a Jeol JEM-2010 (200 kV). XRD patterns of the particle assemblies were collected on a Bruker AXS D8-Advance diffractometer with Cu K $\alpha$  radiation ( $\lambda = 1.5418 \text{ \AA}$ ). UV/vis spectra were recorded on a Perkin Elmer Lambda 35 spectrometer. STEM and elemental analysis were carried out on FEI Tecnai F20ST analytical electron microscopy at Argonne National Laboratory. Additional analyses were done with JEOL 2200FS TEM/STEM at Oak Ridge National Laboratory equipped with a CEOS aberration (probe) corrector. The microscope was operated at 200kV in high angle annular dark field (HAADF) scanning transmission electron microscopy (STEM) mode. The probe size was  $\sim 0.7 \text{ \AA}$  and probe current was  $\sim 30 \text{ pA}$  during HAADF-STEM imaging. When accumulating EDS data, to increase probe current to  $\sim 400\text{-}500 \text{ pA}$ , the probe size was  $\sim 2 \text{ \AA}$ . A Bruker-AXS X-Flash 5030 silicon drift detector was the EDS system.

### 5.7.1.3 Electrochemical Study

The catalysts were dispersed in deionized water (double-filtered, Milli-Q,  $\rho \geq 18.2 \text{ M}\Omega \text{ cm}$ ) by sonication. A drop of the catalyst suspensions was deposited onto a glassy carbon disk (6 mm in diameter) and dried in Ar stream. The Pt loading was  $15 \text{ \mu g/cm}^2$  (Pt/disk) in all cases. All cyclic voltammograms and polarization curves were recorded with sweep rates of 20 and 50 mV/s using an Autolab 302 electrochemical analyzer. 0.1 M perchloric acid (prepared by diluting ultra pure perchloric acid (70%, OmniTrace Ultra<sup>TM</sup>, EMD) with deionized water) was used as the electrolyte. The prolonged potential cycling was done at 20°C in order to diminish the influence of contaminants and electrolyte evaporation, which could be significant at elevated temperatures. All potentials are given versus reversible hydrogen electrode (RHE).

### 5.7.1.4 Theory and Simulations

The DACAPO code [40] was used for all total energy calculations in this study. A four-layer slab, periodically repeated in a super cell geometry with six equivalent layers of vacuum between any two successive metal slabs, was used; the RPBE [40]-optimized Pt<sub>3</sub>Fe lattice constant is 3.96 Å. A (2x2) unit cell was employed. The top two layers of the slab were allowed to relax until the total force on all atoms was less than 0.04 eV/Å in any Cartesian direction. Adsorption was allowed on one of the two exposed surfaces

of the metal slabs, and the electrostatic potential was adjusted accordingly [41]. Ionic cores were described by ultrasoft pseudopotentials [42], and the Kohn-Sham one-electron valence states were expanded in a basis of plane waves with kinetic energy below 340 eV; a density cutoff of 500 eV was used. The surface Brillouin zone was sampled with an 18 Chadi-Cohen  $\mathbf{k}$  point grid. The convergence of the total energy with respect to the cut-off energies and the  $\mathbf{k}$  point set was confirmed. The exchange-correlation energy and potential were described by the generalized gradient approximation (GGA-RPBE) [42]. The self-consistent RPBE density was determined by iterative diagonalization of the Kohn-Sham Hamiltonian, Fermi population of the Kohn-Sham states ( $k_B T = 0.1$  eV), and Pulay mixing of the resulting electronic density [43]. All total energies were extrapolated to  $k_B T = 0$  eV.

## 5.7.2 Part 2 Electrochemical Properties of Well-Defined Surfaces

### 5.7.2.1 Electrochemical characterization of Pt and FePt<sub>3</sub> thin films on Au(111) substrate

#### 5.7.2.1.1 Au(111)-Pt

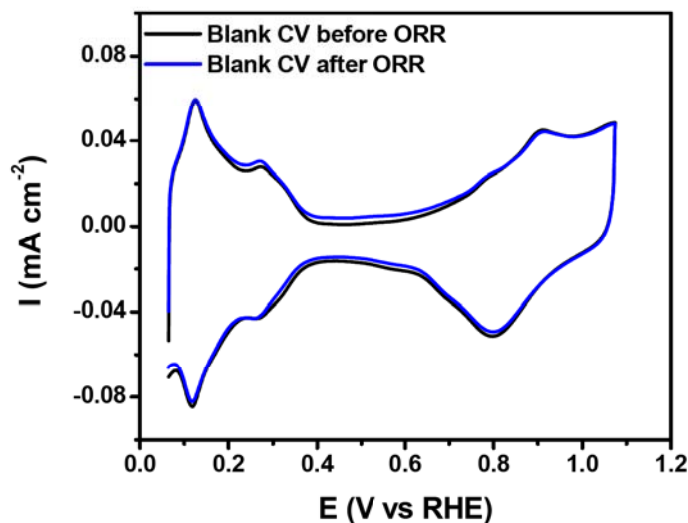


Figure 5.14. Blank CV for 1.5 nm Pt thin film supported on Au(111) before (black), and after (blue) ORR measurements at 20 and 60°C. The integrated charge of  $H_{\text{upd}}$  is found to be  $210 \mu\text{Ccm}^{-2}$ , which is equal to the expected value for polycrystalline Pt surface.

The cyclic voltammogram of the Au(111)-Pt surface in Ar saturated electrolyte is identical before and after the ORR experiments. No change in integrated charge of underpotentially deposited hydrogen ( $H_{\text{upd}}$ ) demonstrates stable behavior of Pt atoms on the Au substrate, confirming that the surface composition stays the same.

Electro-oxidation of the fully covered CO adlayer over Au(111)-Pt surface revealed that the integrated charge from the CO stripping peak of  $420 \mu\text{Ccm}^{-2}$  matches the surface area obtained from  $H_{\text{upd}}$ . That was additional confirmation that surface was fully covered with Pt atoms. In addition, cyclic voltammetry does not change before and after experiments with CO indicating that the surface composition is not affected.

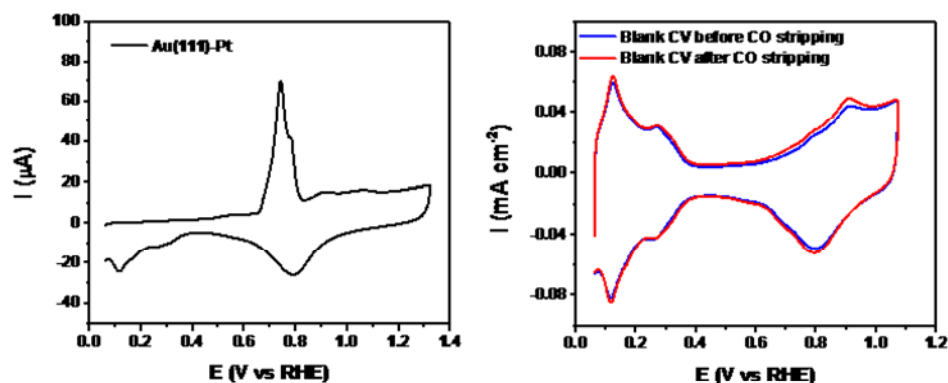


Figure 5.15. (a) CO stripping performed on Au(111)-Pt thin film. The integrated charge of CO stripping is  $420 \mu\text{Ccm}^{-2}$ , which is a perfect match with expected value for polycrystalline Pt. (b) Blank CV measured before (blue) and after (red) CO stripping. They are similar to each other, and the  $H_{\text{upd}}$  region is identical showing no reduction in exposed Pt surface area.

#### 5.7.2.1.2 Au(111)-FePt<sub>3</sub>

Cyclic voltammetry of Au(111)-FePt<sub>3</sub> in Ar saturated electrolyte does not change before and after the ORR experiments, Figure 5.16. The  $H_{\text{upd}}$  features are broader than in the Au(111)-Pt thin film, with the integrated charge density of  $180 \mu\text{Ccm}^{-2}$ , which is lower than that of Au(111)-Pt. This fits with previous results obtained on bulk alloys [13] in which the  $H_{\text{upd}}$  region of Pt-bimetallic alloy surfaces was found to be lower than that of polycrystalline Pt. Additionally, no change in integrated charge of  $H_{\text{upd}}$  demonstrates stable behavior of Pt atoms on the Au substrate, confirming that surface composition of Pt-bimetallic thin film stays the same.

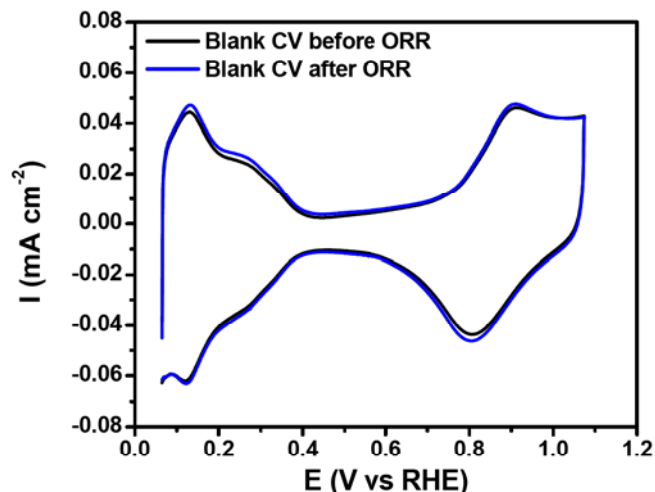


Figure 5.16. Blank CV for Au(111)-FePt<sub>3</sub> thin film before (black) and after (blue) ORR measurements at 20 and 60°C. Similar to the Pt film on gold, from the absence of change in  $H_{\text{upd}}$  area it can be determined that there was no loss of Pt surface area during measurement of the ORR.

Electro-oxidation of a fully covered CO adlayer on the Au(111)-FePt<sub>3</sub> surface revealed that the integrated charge from the CO stripping peak of 420  $\mu\text{Ccm}^{-2}$  matches the surface area obtained from Au(111)-Pt and polycrystalline Pt surfaces. The difference between the integrated charges for  $H_{\text{upd}}$  and CO stripping originates from altered electronic properties of the Pt topmost atoms. Due to changed electronic/adsorption properties [13] only the total charge of  $H_{\text{upd}}$  is affected - decreased with about 30  $\mu\text{Ccm}^{-2}$ , while total coverage of  $\text{CO}_{\text{ad}}$  due to strong Pt-CO interaction remains the same as in the case of pure Pt surfaces. This is additional confirmation that the Pt-bimetallic thin film completely covered the geometric surface area of the Au(111) substrate. In addition, cyclic voltammetry does not change before and after experiments with CO, indicating that the surface coverage of Pt atoms stays the same.

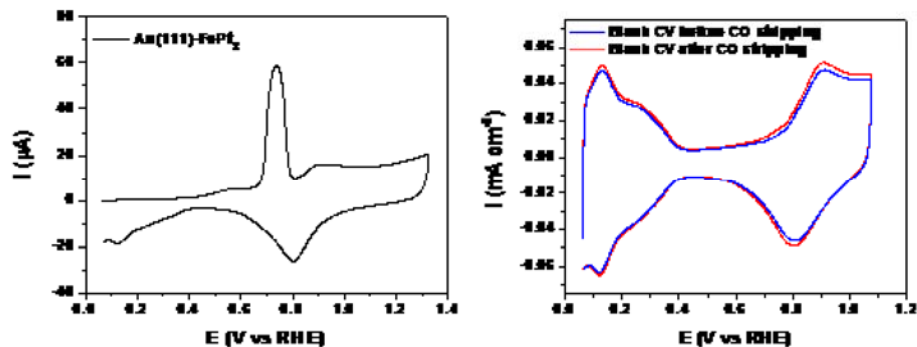
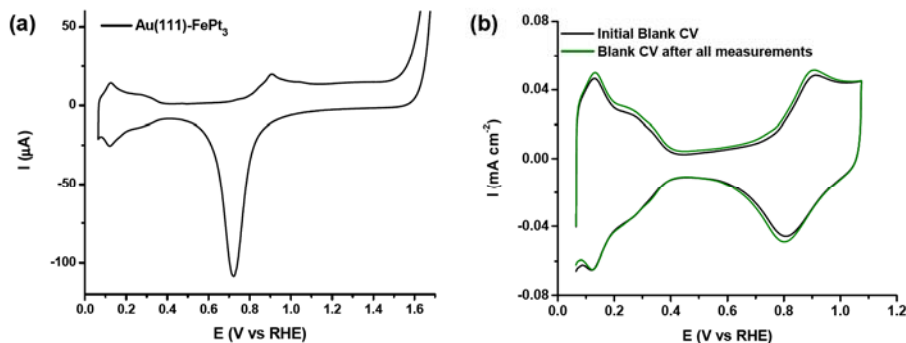


Figure 5.17. (a) CO stripping performed on Au(111)-FePt<sub>3</sub> thin film, showing a single CO stripping feature. The integrated charge of CO stripping is 420  $\mu\text{Ccm}^{-2}$ , equal to the values obtained on Au(111)-Pt and polycrystalline Pt. (b) Blank CVs measured before and after CO stripping show that the H<sub>upd</sub> region is identical without reduction in exposed Pt surface area.

### 5.7.2.1.3 The absence of Au atoms on the Au(111)-FePt<sub>3</sub> surface

Figure 5.1 summarizes the electrochemical characterization of well-defined extended thin film surfaces on the Au(111) substrate. From this summary it is obvious that, in accordance with the electrochemical property of the individual elements, addition of each of these metals induces extra functionality in the catalyst. In addition, the Au surface atoms are chemically stable in acidic electrolyte and inert towards the adsorption/desorption processes of H<sub>upd</sub> (region I), while reversible adsorption/desorption of surface oxides is evident in the region IV between  $1.1 < E < 1.6$  V. This redox couple at 1.35 V and 1.15 V could be effectively used as a signature for the presence of Au surface atoms. In order to make a systematic electrochemical analysis of these thin film surfaces, we extended the potential window up to 1.65 V vs. reversible hydrogen potential. In figure 5.18, a voltammogram of Au(111)-FePt<sub>3</sub> is shown, which was recorded in the extended potential region. No detectable peaks that would indicate the presence of Au were found.



**Figure 5.18.** (a) CV for Au(111)-FePt<sub>3</sub> thin film with 1.5 nm thickness by opening the potential to 1.65V. The CV does not show characteristic features for the presence of surface Au. (b) Comparison of CVs before (black curve) and after (green curve) ORR at 20 and 60°C, CO stripping and increasing the upper potential limit measurements.

In addition, comparison between CVs (figure 5.18b) before and after the whole series of electrochemical measurements, such as ORR at 20 and 60°C, CO stripping and measurements in an extended potential range up to 1.65 V, confirms that during the course of the measurements the  $H_{\text{upd}}$  area has not changed and the thin Pt-bimetallic film remains stable without noticeable change in surface composition.

In order to demonstrate that Au surface atoms could be detected if they are exposed to the electrolyte we performed electrochemical measurements with a different film thickness. Based on these results it was possible to conclude that surfaces of FePt<sub>3</sub> films that are thinner than 1 nm have some Au atoms on the surface. This is clearly visible from the cyclic voltammetry in figure 5.19, where the Au oxidation is clearly visible, indicating the presence of Au surface atoms. From the integrated  $H_{\text{upd}}$  charge of  $170 \mu\text{Ccm}^{-2}$  it was estimated that the Au surface composition was about 5%. This example confirms that this methodology can be efficiently used to detect Au surface atoms.

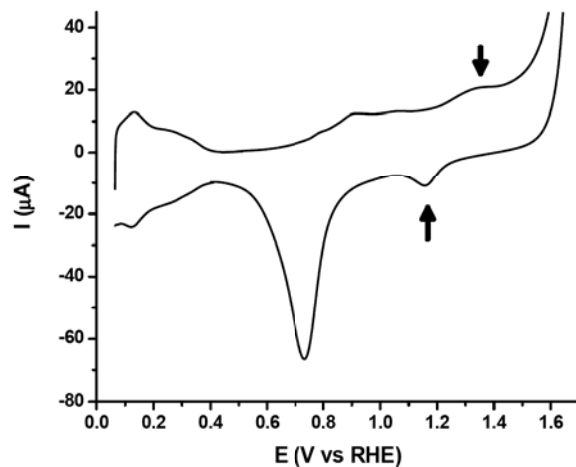


Figure 5.19. CV for Au(111)-FePt<sub>3</sub> thin film of <1 nm by opening the potential to 1.65V. It shows clearly that, in contradictory to Au(111)-FePt<sub>3</sub> thin film of 1.5 nm shown above, some gold is exposed on the surface as seen by the Au-OH<sub>ad</sub> redox couple at 1.35V and 1.15 V.

### 5.7.3 Part 3 Properties of Multimetallic Nanoparticles

#### 5.7.3.1 Elemental analysis of Au/FePt<sub>3</sub> nanoparticles:

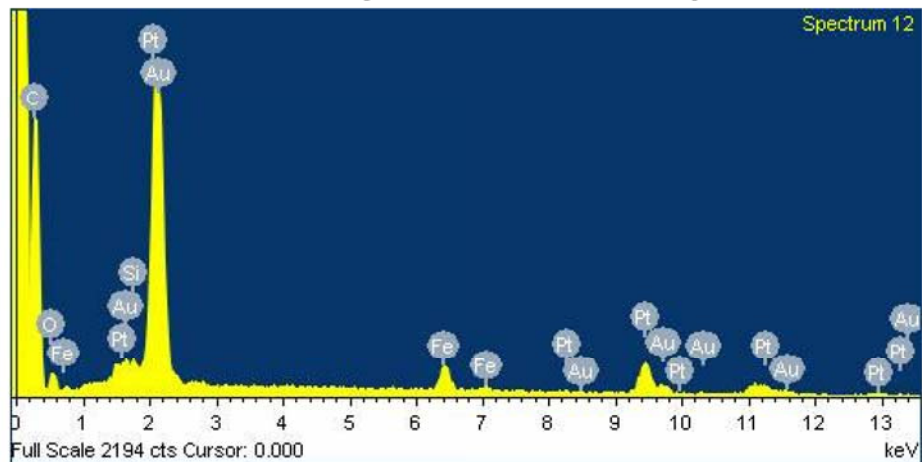
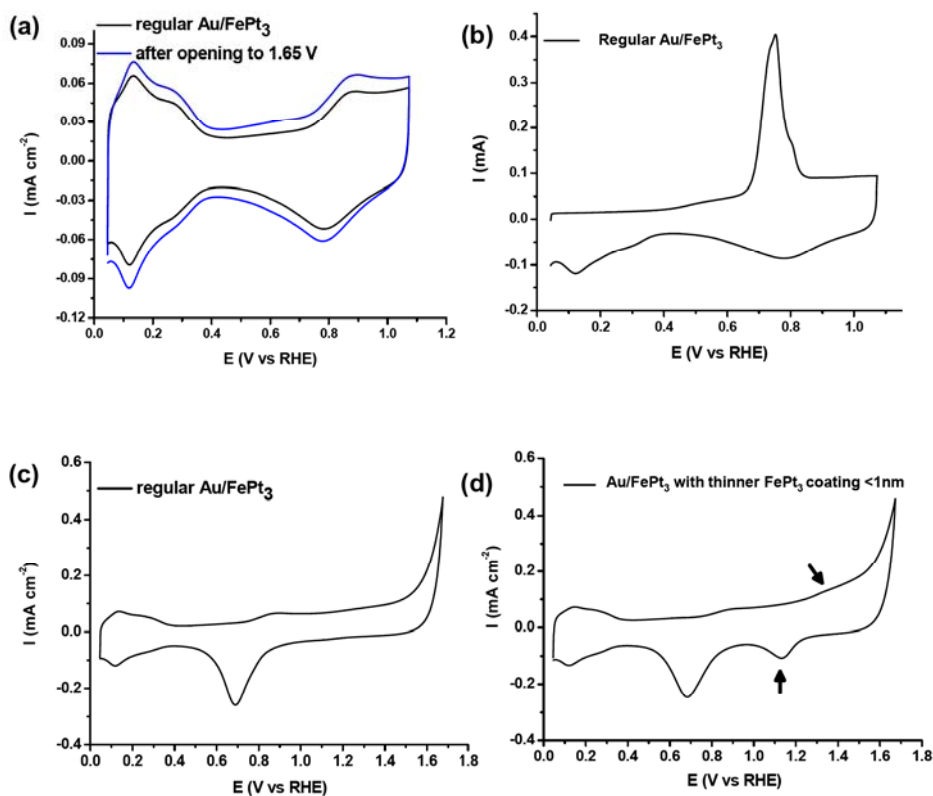


Figure 5.20. EDX pattern of Au/FePt<sub>3</sub> NPs. The atomic composition of the NPs is Au 28%, Fe 17%, and Pt 55%.

## 5.7.3.2 Electrochemical Characterization



**Figure 5.21.** Electrochemical characterization of Au/FePt<sub>3</sub>/C nanoparticle catalyst. (a) CVs before and after electrochemical characterizations (no surface atoms of Au after opening potential to 1.65 V); (b) CO stripping curve for regular 7/1.5 nm Au/FePt<sub>3</sub>/C NPs; (c) and (d) CVs recorded for regular and Au/FePt<sub>3</sub>/C with thinner FePt<sub>3</sub> coating catalysts respectively by opening the upper potential limit to 1.65 V.

The integrated  $H_{\text{upd}}$  charge obtained from regular particles was found to be in perfect agreement with the charge calculated from CO stripping. In figure 5.21a, CVs before and after electrochemical characterizations for ORR at 20 and 60°C, CO stripping and measurements in extended potential range up to 1.65 V, confirm that during the course of the measurements the  $H_{\text{upd}}$  area has not changed and the Pt-bimetallic coating remains stable without noticeable change in surface composition. However, the double layer region has increased (blue curve in insert a) after opening and cycling potential to 1.65 V. This is due to the oxidation and consecutive roughening of the carbon support at elevated potentials. A very

important finding is given in figure 5.21c, which depicts that no Au features are visible in the CV with upper potential opened to 1.65 V, confirming the formation of stable Pt surface free of any Au atoms.

We investigated another type of Au/FePt<sub>3</sub> NPs with bimetallic coating thickness less than 1.0 nm, which were obtained by controlled synthesis with reduced precursors (0.05 g Pt(acac)<sub>2</sub> and 0.015 ml Fe(CO)<sub>5</sub>) and lower growth temperature (180°C). The particles with thinner coating, however, show characteristic gold features in the CV when the upper potential limit is opened to 1.65 V (figure 5.21d), indicating that PtM-coating does not completely encapsulate Au core. This illustrates that, if present on the NP surface, Au atoms could be detected by cyclic voltammetry.

## 5.7.4 Part 4 Mechanism of Stability Enhancement

### 5.7.4.1 Nanoparticle Shape

Table 5.1. Theoretical calculation of average coordination number of surface atoms for different shape of nanoparticles of 10 nm in size.

Coordination number	Cubo-octahedron [44-46]	Icosahedron [47]
6	24	12
7	396	0
8	726	570
9	3176	3420
10	0	0
11	0	0
Total number of surface atoms	4322	4002
Average coordination number	8.632	8.849

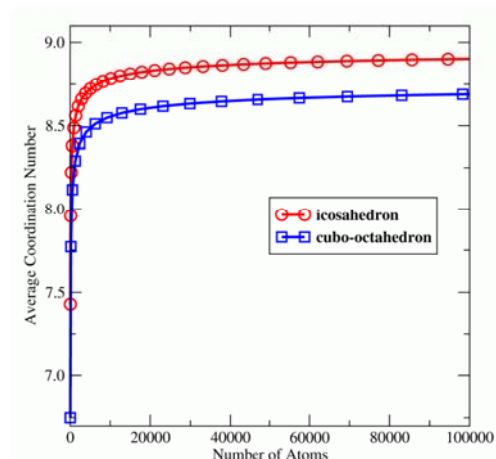


Figure 5.22. Average coordination number of the surface atoms varies as a function of the total number of atoms in the particles with a cubo-octahedral, or icosahedral shape.

#### 5.7.4.2 Stability enhancement through adsorbate induced segregation of Pt

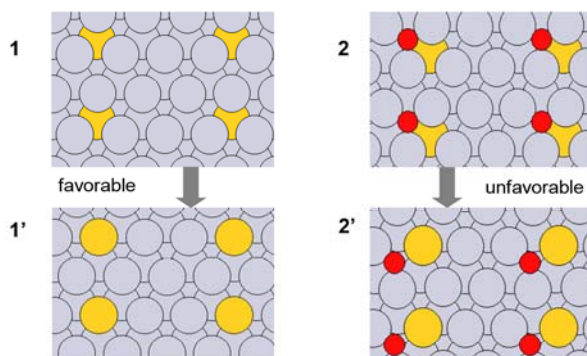
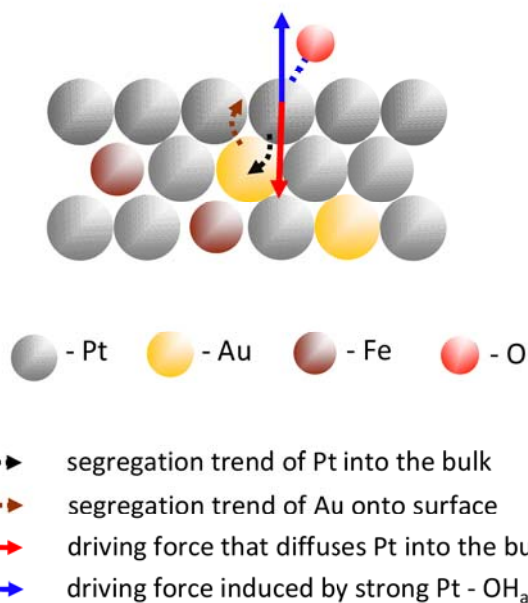


Figure 5.23. (*Top view*) Density Functional Theory calculations of subsurface and surface Au atoms on a Pt(111) surface: (1-1') A top view of Au segregation from the subsurface to the surface layer; the energy change for this process is  $\sim -0.4$  eV in vacuum (thermodynamically favorable). (2-2') A top view of Au segregation from the subsurface to the surface layer in the presence of adjacent oxygen on the surface. The segregation energy in this case is  $\geq 0.0$  eV (thermodynamically unfavorable), and Au atoms movement to the surface is suppressed. Higher coverages of oxygen (as would be observed at elevated electrode potentials) are expected to further inhibit the movement of Au to the surface. All calculations are done on a (3x2), 5-layer unit cell with the top three layers relaxed. The RPBE functional is used with a Monkhorst-Pack k-point grid of (3,4,1); ultrasoft pseudopotentials are employed, and a planewave cutoff of 340 eV (density cutoff of 500 eV) is also used.

Gray spheres denote Pt, yellow denotes Au and red denotes O.

Pt is much more oxophilic than Au, this means that Pt surface atoms oxidize at more negative potentials than Au surface atoms. The onset of oxide adsorption on Au is shifted positively with more than 600 mV (figure 5.1a).



**Figure 5.24. (Side View) Schematic illustration of the stability enhancement mechanism**

Au atoms tend to segregate on the surface due to the lower surface energy of Au than Pt, but under the given electrochemical conditions ( $0.6 < E < 1.1$  V), oxygenated species (*e.g.*, O, OH) are binding strongly to surface Pt, which provide the driving force for Pt atoms to stay on the surface in the highly oxophilic environment. Such a counterbalance between the two opposing forces (see figure 5.24); the rather strong interaction between Pt and surface oxides on one side, and the tendency of Au to segregate over Pt on the other side, stabilizes of the topmost Pt layer.

### 5.7.4.3 Stabilization of Pt surface atoms through the hindered place exchange mechanism

Gold cannot be oxidized in the given potential range that is relevant for the ORR ( $0.6 < E < 1.2$  V), and therefore occurrence of Au in the subsurface layers would make the formation of subsurface oxides less energetically favorable and hence suppress the dissolution of Pt.

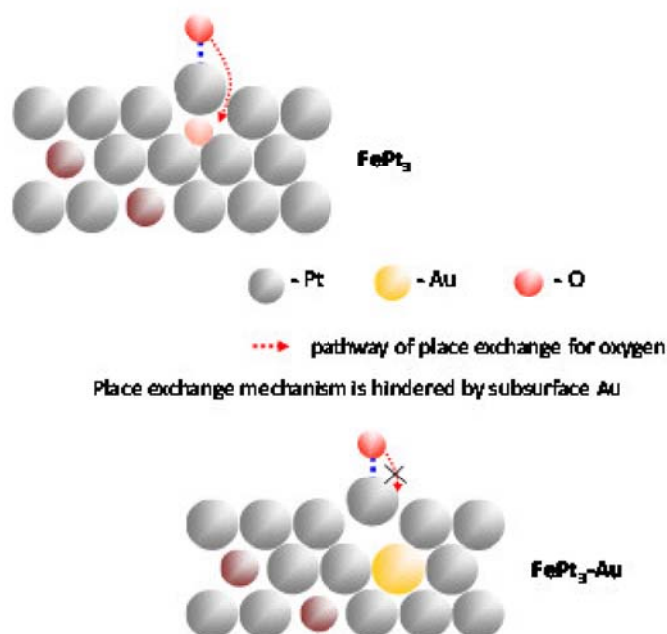


Figure 5.25. (Side View) Schematic illustrations of stability enhancement mechanism of Pt surface atoms in multimetallic NPs

#### 5.7.4.4 DFT calculations of the subsurface atomic oxygen adsorption in FePt<sub>3</sub>(111) alloys with subsurface Au

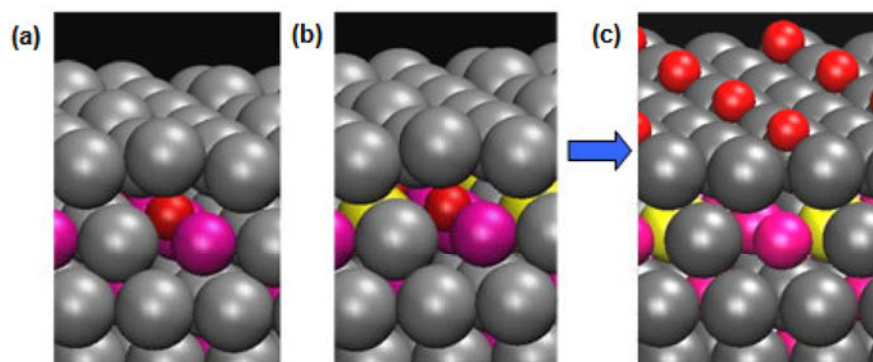


Figure 5.26. (Side View) Most favorable absorption of subsurface oxygen. (a) FePt<sub>3</sub> alloy with 0.5 ML of Fe in the first subsurface layer. (b) Au/FePt<sub>3</sub> alloys with 0.5 ML of Fe and 0.25 ML of Au in the first subsurface layer. (c), the overall thermodynamic driving force for subsurface oxygen formation. Gray spheres denote Pt, yellow denotes Au, red denotes O, and magenta denotes Fe.

Figure 5.26 (a) corresponds to a classic Pt skin-type structure. When a Au atom is substituted for Pt in the subsurface layer (b), the strength of subsurface oxygen adsorption decreases in magnitude by about 0.15 eV. Since the corresponding strength of surface Pt-oxygen binding is nearly the same in both cases, the overall thermodynamic driving force for subsurface oxygen formation (i.e., the subsurface minus the surface oxygen binding energies) also decreases in magnitude by a comparable amount due to the presence of subsurface Au. Oxygen place exchange thus becomes thermodynamically less favorable, thereby reducing Pt loss in the ternary system under this well-known Pt-dissolution mechanism.

## References

- [1] W. Vielstich, A. Lamm, and H. A. Gasteiger, *Handbook of fuel cells : fundamentals, technology, and applications*, Wiley, Chichester, England ; Hoboken, N.J., 2003.
- [2] B. Richter, D. Goldston, G. Crabtree, L. Glicksman, D. Goldstein, D. Greene, D. Kammen, M. Levine, M. Lubell, M. Savitz, D. Sperling, F. Schlachter, J. Scofield, and J. Dawson, *Reviews of Modern Physics*. 80 (2008) S1.
- [3] P. J. Ferreira, G. J. la O', Y. Shao-Horn, D. Morgan, R. Makharia, S. Kocha, and H. A. Gasteiger, *Journal of the Electrochemical Society*. 152 (2005) A2256.
- [4] A. J. Appleby, *Catal. Rev.* 4 (1971) 221.
- [5] T. Toda, H. Igarashi, H. Uchida, and M. Watanabe, *Journal of the Electrochemical Society*. 146 (1999) 3750.
- [6] U. A. Paulus, A. Wokaun, G. G. Scherer, T. J. Schmidt, V. Stamenkovic, V. Radmilovic, N. M. Markovic, and P. N. Ross, *Journal of Physical Chemistry B*. 106 (2002) 4181.
- [7] H. A. Gasteiger, S. S. Kocha, B. Sompalli, and F. T. Wagner, *Applied Catalysis B-Environmental*. 56 (2005) 9.
- [8] S. Guerin, B. E. Hayden, C. E. Lee, C. Mormiche, and A. E. Russell, *Journal of Physical Chemistry B*. 110 (2006) 14355.
- [9] H. T. Duong, M. A. Rigsby, W. P. Zhou, and A. Wieckowski, *Journal of Physical Chemistry C*. 111 (2007) 13460.
- [10] S. Koh, J. Leisch, M. F. Toney, and P. Strasser, *Journal of Physical Chemistry C*. 111 (2007) 3744.
- [11] A. U. Nilekar, Y. Xu, J. L. Zhang, M. B. Vukmirovic, K. Sasaki, R. R. Adzic, and M. Mavrikakis, *Topics in Catalysis*. 46 (2007) 276.
- [12] V. R. Stamenkovic, B. Fowler, B. S. Mun, G. F. Wang, P. N. Ross, C. A. Lucas, and N. M. Markovic, *Science*. 315 (2007) 493.
- [13] V. R. Stamenkovic, B. S. Mun, M. Arenz, K. J. J. Mayrhofer, C. A. Lucas, G. F. Wang, P. N. Ross, and N. M. Markovic, *Nature Materials*. 6 (2007) 241.
- [14] J. Greeley and J. K. Norskov, *Journal of Physical Chemistry C*. 113 (2009) 4932.
- [15] V. Stamenkovic, B. S. Mun, K. J. J. Mayrhofer, P. N. Ross, N. M. Markovic, J. Rossmeisl, J. Greeley, and J. K. Norskov, *Angewandte Chemie-International Edition*. 45 (2006) 2897.
- [16] J. Zhang, K. Sasaki, E. Sutter, and R. R. Adzic, *Science*. 315 (2007) 220.

- [17] Y. Shao-Horn, W. C. Sheng, S. Chen, P. J. Ferreira, E. F. Holby, and D. Morgan, *Topics in Catalysis*. 46 (2007) 285.
- [18] V. Komanicky, K. C. Chang, A. Menzel, N. M. Markovic, H. You, X. Wang, and D. Myers, *Journal of the Electrochemical Society*. 153 (2006) B446.
- [19] D. S. Strmcnik, D. V. Tripkovic, D. van der Vliet, K. C. Chang, V. Komanicky, H. You, G. Karapetrov, J. Greeley, V. R. Stamenkovic, and N. M. Markovic, *Journal of the American Chemical Society*. 130 (2008) 15332.
- [20] J. Luo, L. Wang, D. Mott, P. N. Njoki, Y. Lin, T. He, Z. Xu, B. N. Wanjana, I. I. S. Lim, and C. J. Zhong, *Advanced Materials (Weinheim, Germany)*. 20 (2008) 4342.
- [21] T. Ghosh, M. B. Vukmirovic, F. J. DiSalvo, and R. R. Adzic, *Journal of the American Chemical Society*. 132 (2010) 906.
- [22] S. Peng, Lee, Y., Wang, C., Yin, H., Dai, S., Sun, S., *Nano Research*. 1 (2008) 229.
- [23] T. J. Schmidt, V. Stamenkovic, M. Arenz, N. M. Markovic, and P. N. Ross, *Electrochimica Acta*. 47 (2002) 3765.
- [24] F. Tao, M. E. Grass, Y. W. Zhang, D. R. Butcher, J. R. Renzas, Z. Liu, J. Y. Chung, B. S. Mun, M. Salmeron, and G. A. Somorjai, *Science*. 322 (2008) 932.
- [25] D. Ferrer, A. Torres-Castro, X. Gao, S. Sepulveda-Guzman, U. Ortiz-Mendez, and M. Jose-Yacamán, *Nano Letters*. 7 (2007) 1701.
- [26] X. M. Lu, H. Y. Tuan, J. Y. Chen, Z. Y. Li, B. A. Korgel, and Y. N. Xia, *Journal of the American Chemical Society*. 129 (2007) 1733.
- [27] Z. M. Peng, J. B. Wu, and H. Yang, *Chemistry of Materials*. 22 (2010) 1098.
- [28] S. H. Sun, C. B. Murray, D. Weller, L. Folks, and A. Moser, *Science*. 287 (2000) 1989.
- [29] K. Kinoshita, *Journal of the Electrochemical Society*. 137 (1990) 845.
- [30] K. J. J. Mayrhofer, B. B. Blizanac, M. Arenz, V. R. Stamenkovic, P. N. Ross, and N. M. Markovic, *Journal of Physical Chemistry B*. 109 (2005) 14433.
- [31] C. e. a. Wang, *J. Phys. Chem. C*. (2009).
- [32] E. F. Holby, W. C. Sheng, Y. Shao-Horn, and D. Morgan, *Energy & Environmental Science*. 2 (2009) 865.
- [33] Z. L. Wang, *Journal of Physical Chemistry B*. 104 (2000) 1153.
- [34] B. Lim, J. G. Wang, P. H. C. Camargo, M. J. Jiang, M. J. Kim, and Y. N. Xia, *Nano Letters*. 8 (2008) 2535.
- [35] S. E. Habas, H. Lee, V. Radmilovic, G. A. Somorjai, and P. Yang, *Nature Materials*. 6 (2007) 692.
- [36] M. C. Daniel and D. Astruc, *Chemical Reviews*. 104 (2004) 293.
- [37] N. Kimizuka, T. Abe, and K. Itaya, *Denki Kagaku*. 61 (1993) 796.
- [38] A. V. Ruban, H. L. Skriver, and J. K. Nørskov, *Physical Review B*. 59 (1999) 15990.
- [39] H. You, D. J. Zurawski, Z. Nagy, and R. M. Yonco, *Journal of Chemical Physics*. 100 (1994) 4699.
- [40] B. Hammer, L. B. Hansen, and J. K. Nørskov, *Phys. Rev. B*. 59 (1999) 7413.
- [41] L. Bengtsson, *Physical Review B*. 59 (1999) 12301.
- [42] D. Vanderbilt, *Phys. Rev. B*. 41 (1990) 7892.
- [43] G. Kresse and J. Furthmüller, *Comput. Mater. Sci*. 6 (1996) 15.
- [44] G. F. Wang, M. A. Van Hove, P. N. Ross, and M. I. Baskes, *Journal of Chemical Physics*. 121 (2004) 5410.
- [45] G. F. Wang, M. A. Van Hove, P. N. Ross, and M. I. Baskes, *Journal of Physical Chemistry B*. 109 (2005) 11683.

*Chapter 5*

- [46] G. F. Wang, M. A. Van Hove, P. N. Ross, and M. I. Baskes, *Journal of Chemical Physics*. 122 (2005).
- [47] C. L. Cleveland and U. Landman, *Journal of Chemical Physics*. 94 (1991) 7376.